Keyhole Resonators for Subwavelength Focusing of Microwave Magnetic Fields in Optically Detected Electron Spin Resonance

E.A. Chekhovich ⬤*

Department of Physics and Astronomy, University of Sheffield, Sheffield S3 7RH, United Kingdom

Microwave resonators with a keyhole profile (KHRs) operating in the C band and the X band are designed and studied in numerical simulations and experiments. KHR structures concentrate a microwave magnetic field in a subwavelength volume, while suppressing microwave electric fields. This microwave magnetic field is focused at a finite working distance from KHR metal structures, allowing convenient optical excitation of the sample in both the Faraday geometry and the Voigt geometry. By means of room-temperature optically detected electron spin resonance on SiC quantum defects, the conversion factor $B_1 P_{\mathrm{MW}}^{-1/2}$ for conversion of microwave power into a microwave magnetic field is measured to be approximately 1.0×10^{-3} T W$^{-1/2}$ at a frequency of approximately 7 GHz and a working distance of approximately 0.5 mm from the KHR structure. Numerical simulations match the experimental observations, and an example model code for use with the finite-element-method program ELMER is provided. The KHR structures are most promising for fast coherent electron-spin control in solid-state spin qubits, where a large microwave magnetic field needs to be achieved with simultaneous suppression of microwave heating and electric fields, while permitting efficient optical spin initialization and readout.

I. INTRODUCTION

Resonating elements are used in spectrometers to increase the amplitude of the oscillating field and increase the sensitivity in electron-spin-resonance (ESR) spectroscopy. For conventional ESR spectroscopy in the X band, a TE$_{102}$ rectangular cavity is a commonly used resonator. This type of cavity has dimensions comparable to the wavelength λ of the electromagnetic field and performs well in continuous-wave (cw) spectroscopy due to its high quality factors ($Q \approx 1000$–$10\,000$). In pulsed magnetic resonance spectroscopy, loop-gap resonators (LGRs) [1–3] are advantageous due to their smaller Q of approximately 100–1000, allowing shorter microwave (MW) pulses. The smaller (subwavelength) mode volume of a LGR is also beneficial as it results in a higher microwave-field conversion factor (magnetic field intensity for a given microwave power). In the past two decades, new applications of magnetic resonance have emerged, such as coherent control of the quantum states of individual electron and nuclear spins for sensing [4–6] and quantum-information processing [6–16]. In these applications oscillating magnetic fields are often applied to the structure in combination with optical excitation and probing, and the requirements for resonator circuits differ from those encountered in conventional magnetic resonance spectroscopy.

The aim of this work is to design resonant circuits suitable for C-band (4–8-GHz) and X-band (8–12-GHz) frequencies and optimized for coherent control of electron spins with simultaneous optical spin manipulation. In particular, the setting sketched in Figs. 1(a)–1(c) is considered, where the direction of the oscillating microwave magnetic field (B_1) needs to be orthogonal to the direction of the optical beam, as often required in semiconductor nanostructures [7,9,17–24]. This scenario requires careful design consideration to achieve large microwave fields without blocking the optical path. The type of structure designed and tested experimentally here is dubbed a keyhole resonator (KHR) due to its characteristic shape, and is optimized to perform well for simultaneous microwave and optical spin control. The setup based on the KHR and designed in this work essentially operates as a dual-band microscope capable of contactless microwave and optical sample excitation.

Before we proceed to the results and discussion, a list of different performance objectives arising in microwave resonator design is given, and the ways these are taken into account in KHR design are highlighted:

(a) Maximized microwave-magnetic-field conversion factor (maximized field amplitude B_1 at a given microwave power P_{MW}). The conversion efficiency can be increased by increasing the resonator quality factor Q and/or by reducing the resonator mode volume. The Q factor might
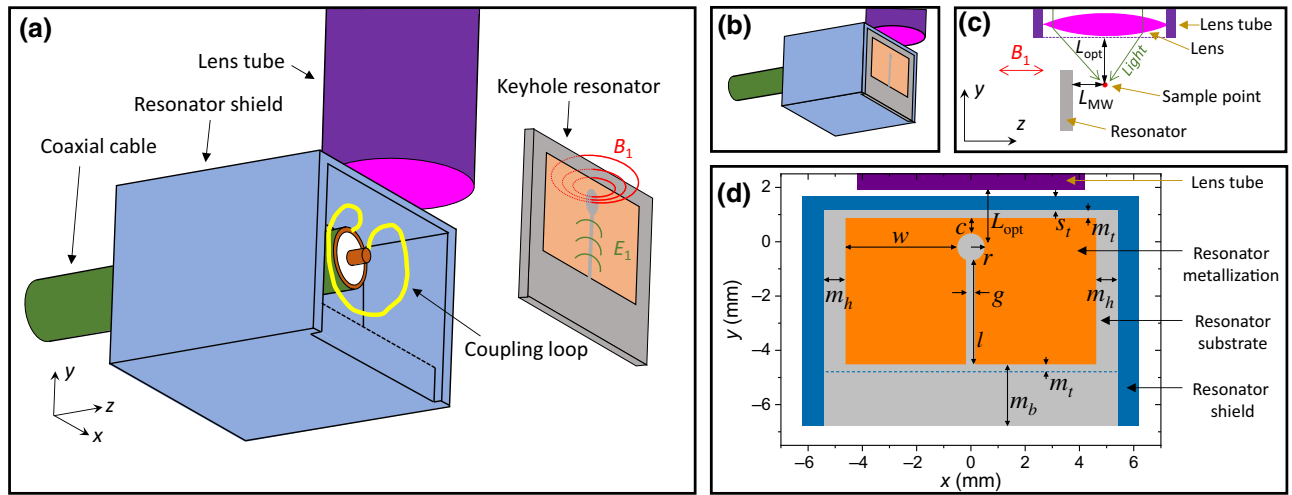
————
*e.chekhovich@sheffield.ac.uk

FIG. 1. (a) The resonator assembly with the KHR removed from the copper shield to reveal the coupling loop connected to the end of the coaxial cable. The KHR consists of a rectangular PTFE substrate and a thin layer of metallization shaped in a keyhole profile. Field lines are shown schematically for magnetic (B_1) and electric (E_1) components in resonance. Optical access is provided by an objective mounted in the lens tube. (b) Keyhole resonator installed in the shield. (c) Keyhole resonator and the lens assembly in the y-z plane. The optical and microwave working distances are L_{opt} and L_{MW}, respectively. The microwave field B_1 is polarized predominantly along the z axis. (d) Dimensions of the keyhole resonator in the x-y plane. The schematic drawing and the specific numerical values in this caption are shown for the KHR-1 model discussed in Section II D. The keyhole profile is formed by a circle of radius $r = 0.5$ mm and a gap of width $g = 0.3$ mm and length $l = 3.8$ mm etched away from the rectangular metallization. The circle is shifted toward the top of the metal rectangle, forming a narrow constriction of width $c = 0.55$ mm between the top of the circle and the metal-rectangle top edge. The narrowest width w of the metal between the side of the rectangle and the side of the circle is 4.1 mm. The top margin m_t (bottom margin m_b) between the metal and the PTFE substrate edge is 0.3 mm (2.6 mm), while the margin in the horizontal x direction is m_h. The dashed line at $y = -4.79$ mm corresponds to the projection of the edge of the resonator shield marked by the dashed line in (a): the gap in the y direction between this line and the bottom edge of the KHR metal equals m_t.

be limited by other design requirements, whereas reduction of the mode volume can be achieved by use of surface resonators [25,26], including split-ring resonators [27–30], surface LGRs, and more-elaborate designs [31–34] with mode dimensions as small as 20 μm, as well as superconducting structures [35]. The KHR is a surface structure with design parameters optimized numerically to achieve optimal conversion efficiency.

(b) Minimized microwave electric field. The presence of the electric field E_1 is undesirable as it results in dielectric losses [36,37], and in quantum-information applications it can create parasitic voltages in charge control and readout lines or hinder spin coherence [38]. In the case of LGRs, bridged structures [36,39,40] are used to shield the sample volume from the electric fields [41]. As with the conversion efficiency, the design parameters of the KHR are optimized numerically to minimize the electric field at the sample location. Moreover, the KHR design avoids direct mechanical contact between the resonator and the sample studied, thus suppressing the microwave heating effects, as well as reducing the microwave electric field and removing the need for additional structures to compensate it [38].

(c) Optical access. Experiments such as optically-detected-magnetic-resonance (ODMR) require unobst-

ructed optical access to the sample with a large numerical aperture (NA). With surface resonators it is straightforward to excite the sample optically with light propagating along the normal to the surface. Since such resonators usually produce an out-of-plane microwave magnetic field B_1, the static magnetic field B_0 must then be parallel to the resonator surface, corresponding to the Voigt geometry. However, ODMR experiments in solid-state nanostructures [7,9,14,20] often require optical excitation parallel to the static magnetic field (Faraday geometry) to enable dynamic spin polarization [17,19] or to exploit chirality effects [21,23]. To avoid obstruction of the optical beam in the Faraday geometry, the sample must be placed at a finite distance L_{MW} from the resonator surface, implying that the conversion efficiency can no longer be increased by simply placing the current-conducting elements close to the sample. KHRs are designed to operate in both the Voigt geometry and the Faraday geometry, and optimization of the microwave-magnetic-field conversion efficiency explicitly takes into account the need for a finite distance between the sample and the resonator.

(d) Radio-frequency transparency. Electron-nuclear double resonance requires simultaneous application of microwave and radio-frequency magnetic fields, which is difficult to achieve in cavity resonators, but is readily

possible with a KHR in the same way it is achieved with other surface resonators and LGRs [36,39].

(e) *Pulsed operation.* A small Q factor is essential for suppressing resonator ringing and allowing short microwave bursts required in pulsed magnetic resonance and coherent electron-spin manipulation [3]. KHR structures have small Q factors on the order of approximately 100, enabling broadband electron-spin control on timescales of just a few tens of nanoseconds.

(f) *Microwave-field homogeneity.* In magnetic resonance applications with bulk samples, it is advantageous to have a uniform amplitude of the microwave magnetic field across the volume of the sample. Good homogeneity can be achieved in LGR structures [36,41]. By contrast, surface resonators designed for a maximized power-to-field conversion factor can have a highly inhomogeneous microwave magnetic field [31] unless this is taken into account in the resonator design [34]. It is shown here that with two KHRs combined (dual-KHR configuration) it is possible to achieve high field homogeneity for planar samples.

(g) *Fabrication complexity.* Planar resonator structures are particularly attractive as they can be produced by lithography and metallization techniques without the need for processes such as accurate cutting or milling. KHR structures operating in the X band can be readily produced by low-cost techniques used for fabrication of printed circuit boards (PCBs).

II. RESONATOR DESIGN AND GEOMETRY OPTIMIZATION

In this section the performance of the resonator structures is examined by numerical simulations. To this end the structures are approximated by means of three-dimensional tetrahedral meshing, and frequency-domain Maxwell equations are solved by the finite-element method, taking into account resistive losses. Magnetic resonator feeding is considered, where a microwave voltage is applied to a wire loop, which is inductively coupled to the resonator (see the Appendix for implementation details and Supplemental Material [42] for code examples). Once the numerical simulation is conducted for a given structure, the amplitudes of the microwave fields at the target excitation frequency f_0 are calculated at the sampling point $(x, y, z) = (0, 0, 0)$. In particular, the amplitude of the MW-magnetic-field z component $B_{1,z}$ and the root-mean-square (rms) amplitudes of the electric field $E_{1,\mathrm{rms}}$ and magnetic field $B_{1,\mathrm{rms}}$ are calculated. As a figure of merit for suppression of the microwave electric field, the ratio $Z_1 = \mu_0 E_{1,\mathrm{rms}}/B_{1,\mathrm{rms}}$ of the fields is used, which has the dimensionality of impedance ($\mu_0 \approx 4\pi \times 10^{-7}$ H m^{-1} is the magnetic constant). A smaller value of Z_1 corresponds to stronger suppression of the microwave electric field for a given magnetic field. The structural parameters

of the resonator and the distance between the resonator and the coupling loop are varied to achieve two-objective optimization (maximize $B_{1,\mathrm{rms}}$ and minimize Z_1) by means of a genetic-type numerical algorithm implemented in Wolfram MATHEMATICA 12.0.

A. LGR reference design and performance

To start with, the standard bridged loop-gap resonator (BLGR) is considered as a reference structure. A sketch of a BLGR with an interior bridge [39] as well as the relevant dimensions are shown in Fig. 2. The full angle of the bridge arc is $\pi/2$. The resonator is fed via inductive coupling to a wire loop (not shown) coaxial with the BLGR. The two-objective optimization is conducted by variation of the parameters r, l, h, and m and sampling of the microwave field at $f_0 = 7.5$ GHz at the geometrical center of the BLGR (a point on the axis of the cylinder, half way through the length h). In the optimization the parameters are allowed to vary within the following constrains: inner-loop radius $r \in [0.25\,\mathrm{mm}, 2.5\,\mathrm{mm}]$, difference between outer and inner radii $l \in [0.1\,\mathrm{mm}, 8.0\,\mathrm{mm}]$, length along the LGR axis $h \in [0.1\,\mathrm{mm}, 6.5\,\mathrm{mm}]$, and insulating spacer thickness $m \in [0.1\,\mathrm{mm}, 2.0\,\mathrm{mm}]$. The gap width g is fixed at 0.3 mm. The circles in Fig. 3 show the result of the two-objective optimization at $f_0 = 7.5$ GHz—the set of points shows an approximation to the Pareto front obtained by maximizing $B_{1,z}$ and minimizing Z_1 (in multiobjective optimization, the Pareto front is a set of points in objective space where improvement of any objective can be achieved only by degrading another objective [43,44]). The maximum conversion factor (microwave-magnetic-field z amplitude $B_{1,z}$ normalized by the square root of the rms microwave power P_{MW}) is found to be approximately 3.4 mT W$^{-1/2}$. Moreover, this systematic optimization
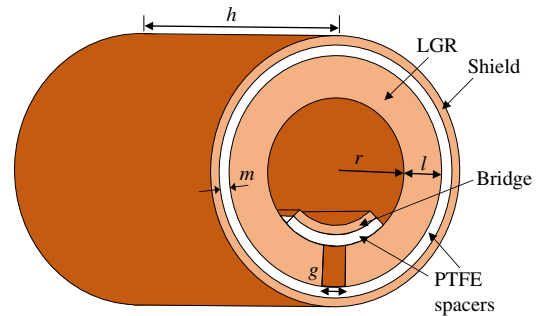
FIG. 2. Schematic drawing of a BLGR with an interior bridge. The inner radius of the copper LGR is r and the difference between the outer and inner radii is l. The width of the gap is g and the length of the LGR along its axis is h. The cylindrical shield is separated from the LGR by a PTFE spacer layer of thickness m. The copper shield, the copper bridge, and the PTFE spacer between the LGR and the bridge have thickness of 0.1 mm.
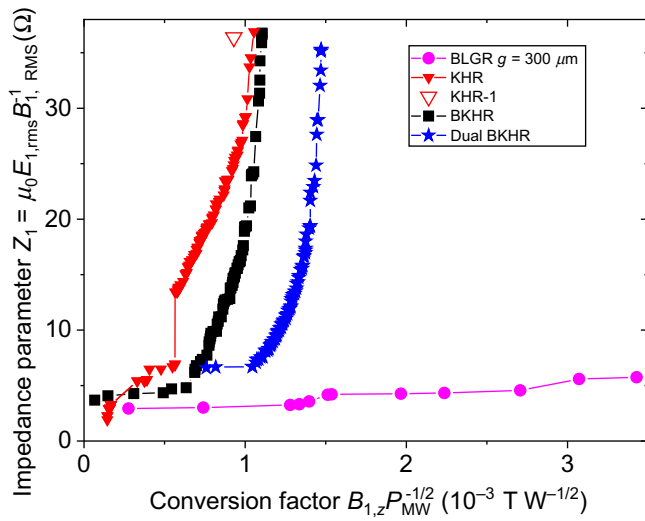
FIG. 3. Results of numerical multiobjective optimization for different resonator structures at microwave excitation frequency $f_0 = 7.5$ GHz. Lines with symbols show Pareto optimal fronts obtained by maximization of the amplitude of the microwave magnetic field $B_{1,z}$ per square root of the input microwave power P_{MW}, and by minimization of the ratio of MW electric and magnetic field amplitudes expressed in terms of the impedance $Z_1 = \mu_0 E_{1,rms}/B_{1,rms}$. The open triangle shows the value for the KHR-1 structure, which is used in detailed simulations and experiments.

shows that the highest $B_{1,z}P_{MW}^{-1/2}$ is achieved at $m \approx 0.8$ mm with large l (approximately 6.4 mm) and small r (approximately 0.26 mm) and h (approximately 0.3 mm), close to the minimums imposed by the optimization constraints. These results show that for a zero-volume (point) sample the maximum conversion efficiency is achieved in a quasiplanar structure ($h \ll r + l$) through close proximity of the current-conducting metallic elements ($r \to 0$). On the basis of these observations, a planar LGR is used as a starting point in the KHR design. However, with a finite constraint on the minimum microwave working distance L_{MW}, the reduction of the radius $r \to 0$ can no longer provide an increase in B_1, resulting in a different optimal geometry for the KHR.

B. KHR design

The schematic of the design is presented in Fig. 1(a), where the main components are shown. A setting is considered where the sample needs to be excited and examined optically—a lens or an objective with high numerical aperture mounted in a tube is used for this purpose with light propagating along the y axis. A coaxial cable is used to deliver microwave power to the coupling loop, which is located inside a solid copper-shield assembly. In the operational state shown in Fig. 1(b), the planar KHR structure is attached to the open side of the shield. The microwave magnetic field is directed predominantly along the z axis.

The geometry of the KHR in the x-y plane is shown in Fig. 1(d) and consists of a rectangular metal layer (orange) on top of a rectangular polytetrafluoroethylene (PTFE) substrate (gray). The keyhole profile is formed by a circle (radius r) and a gap (width g and length l) etched away from the rectangle. The circle is located toward the top of the metal rectangle, forming a narrow constriction of width c between the top of the circle and the metal rectangle. The width of the metallization areas between the sides of the rectangle and the sides of the circle is w. The top (bottom) margin between the metal edge and the PTFE substrate edge is m_t (m_b), while the margin in the horizontal direction is m_h. The projections of the copper shield (blue) and the lens tube (purple) are also shown. The thickness of the top wall of the shield is s_t. Overall, the KHR is derived from the surface LGR geometry with the following modifications. The overall footprint is changed from circular to rectangular for simplified PCB and shield manufacturing. The margin between the metallization of the KHR and the metal-shield assembly is made small, meaning that the KHR itself acts as an additional shield, screening the electric fields produced by the feeding cable and the coupling loop. Finally, unlike the LGR, the KHR shape asymmetrically extends the gap part of the resonator, while maintaining small constriction c in order to allow proximity (from the $y > 0$ direction) of an optical objective with high NA.

The system is designed to permit simultaneous focusing of light and microwaves in a small volume where the sample is located. This sample point is taken to be at $(x, y, z) = (0, 0, 0)$. The bottom edge of the lens tube is taken to be at $y = +1.91$ mm, given by the working distance of the objective lens $L_{opt} = 1.91$ mm [Fig. 1(c)]. The plane of the KHR metallization closest to the sample point is taken to be at $z = -0.52$ mm, which can be described by the effective microwave working distance $L_{MW} = 0.52$ mm [Fig. 1(c)] defining the size (area) of the sample in the x-z plane that can be scanned in an ODMR experiment. These two working distances (optical and microwave) are the main constraints in optimizing the resonator performance while maintaining optical access. In particular, to allow optical access, all current-conducting elements are placed no closer than L_{MW} with respect to the sample point, limiting the achievable microwave magnetic field. These constrains place limitations on the KHR geometry: for example, one requires that $L_{opt} \geq s_t + m_t + c$, and throughout this work $s_t = 0.5$ mm is used.

C. Optimization of KHR geometry

The performance of the keyhole resonators is examined by finite-element numerical simulations. The simulations are conducted for a given structure, and the amplitudes of the microwave fields are calculated at the

sampling point $(x, y, z) = (0, 0, 0)$ for a given optimization frequency f_0 of the microwave excitation. The structural parameters c, w, l, g, r, m_t, and m_h and the distance between the KHR and the coupling loop are varied to achieve two-objective optimization (maximize $B_{1,\mathrm{rms}}$ and minimize Z_1). The parameters are constrained to the values $c \in [0.15 \text{ mm}, 1.0 \text{ mm}]$, $w \in [0.8 \text{ mm}, 5.0 \text{ mm}]$, $l \in [0.3 \text{ mm}, 10.0 \text{ mm}]$, $g \in [0.1 \text{ mm}, 1.4 \text{ mm}]$, $r \in [0.15 \text{ mm}, 1.25 \text{ mm}]$, $m_t \in [0.2 \text{ mm}, 1.5 \text{ mm}]$, and $m_h \in [0.3 \text{ mm}, 6.5 \text{ mm}]$, which can be achieved with standard PCB lithography techniques. The solid triangles in Fig. 3 show the resulting Pareto front for the optimization at $f_0 = 7.5$ GHz. For a KHR assembly constrained with $L_{\mathrm{opt}} = 1.91$ mm and $L_{\mathrm{MW}} = 0.52$ mm, the maximum achievable conversion factor is found to be $B_{1,z} P_{\mathrm{MW}}^{-1/2} \approx 1$ mT W$^{-1/2}$, with the corresponding impedance $Z_1 \approx 37$ Ω—these values are obtained for a structure with $c = 0.3$ mm, $w = 1.5$ mm, $l = 5.7$ mm, $g = 0.5$ mm, $r = 0.56$ mm, $m_t = 0.4$ mm, and $m_h = 3.58$ mm.

From the Pareto fronts, it is found that the KHR provides a lower maximum conversion factor than the BLGR, and the highest $B_{1,z} P_{\mathrm{MW}}^{-1/2}$ is achieved at a larger optimum radius $r = 0.56$ mm, not limited by parameter constrains, but rather comparable to the microwave working distance $r \approx L_{\mathrm{MW}}$. This reduction in $B_{1,z} P_{\mathrm{MW}}^{-1/2}$ quantifies the compromise required for the KHR to focus a microwave field at a finite working distance to permit optical excitation along the y axis, orthogonal to the microwave-field direction z.

D. Resonant modes of the KHR

To investigate the resonant modes of the KHR further, a fixed set of parameters is chosen: $c = 0.55$ mm, $w = 4.1$ mm, $l = 3.8$ mm, $g = 0.3$ mm, $r = 0.5$ mm, $m_t = 0.3$ mm, $m_h = 0.8$ mm, and $m_b = 2.6$ mm, and this design is labeled as "KHR-1". This design, also shown in Fig. 1(d), is marked by an open triangle in Fig. 3 and is close to the Pareto optimal design with maximum $B_{1,z}$. The simulations for KHR-1 presented in this subsection are conducted with higher spatial mesh resolution, which allows better comparison with experiment, but produces slightly different absolute values of resonant frequencies and field amplitudes compared with the optimization simulations shown as Pareto fronts in Fig. 3 and parameter dependencies in Fig. 8. Figure 4(a) shows by the dashed line the simulated power reflection coefficient S_{11} for KHR-1. For the appropriate position of the coupling loop, critical coupling is observed at $f_r \approx 7.543$ GHz. The separation of the -3-dB reflection points is approximately 30 MHz, from which the loaded Q factor Q_L of the resonator is approximately 261. The corresponding unloaded Q factor $Q = 2Q_L \approx 522$ is twice Q_L and describes the intrinsic Q factor of a resonator isolated from the power source (see Sec. 7.2 in Chap. 7 in Ref. [45]). Figure 4(b) shows the simulated microwave-magnetic-field amplitude as a function of the excitation
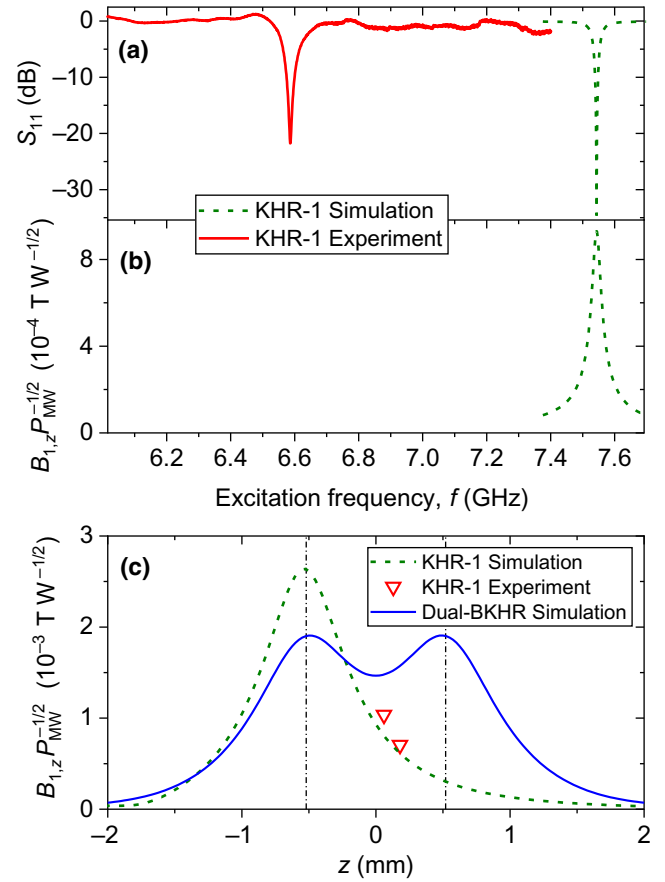

FIG. 4. (a) Power reflection coefficient S_{11} derived from simulations (dashed line) and experiments (thick solid line) for the KHR-1 structure. (b) Frequency dependence of the z component of the microwave-magnetic-field conversion factor $B_{1,z} P_{\mathrm{MW}}^{-1/2}$ at $(x, y, z) = (0, 0, 0)$ derived in simulations. Conversion factor $B_{1,z} P_{\mathrm{MW}}^{-1/2}$ as a function of z coordinate at $(x, y) = (0, 0)$ obtained from simulations for KHR-1 (dashed line) and the dual-BKHR design (thin solid line) and from experiments on KHR-1 (triangles). Dash-dotted lines show positions of the KHR metallization surfaces at $z = \pm L_{\mathrm{MW}}$.

frequency and reveals a peak with a full width at half maximum of approximately 51 MHz.

The two-dimensional cross-section distributions of the microwave electric and magnetic fields calculated under resonant conditions for KHR-1 are presented in Fig. 5. The z component of the microwave magnetic field at $z = 0$ mm [Figs. 5(a) and 5(b)], useful in spin control and magnetic resonance, is concentrated near the circle of the KHR. In particular, the magnetic field lines encircle the narrow constriction of the KHR—this is evidenced in the cross section at $x = 0$ shown in Fig. 5(b), where the largest $B_{1,z}$ is found at the top of the circle $y \approx 0.25$ mm, $z \approx -0.52$ mm, with return flux concentrated in the top margin between the metallization of the KHR and the shield at $y \approx 1.0$ mm, $z \approx -0.52$ mm. In the sample point plane
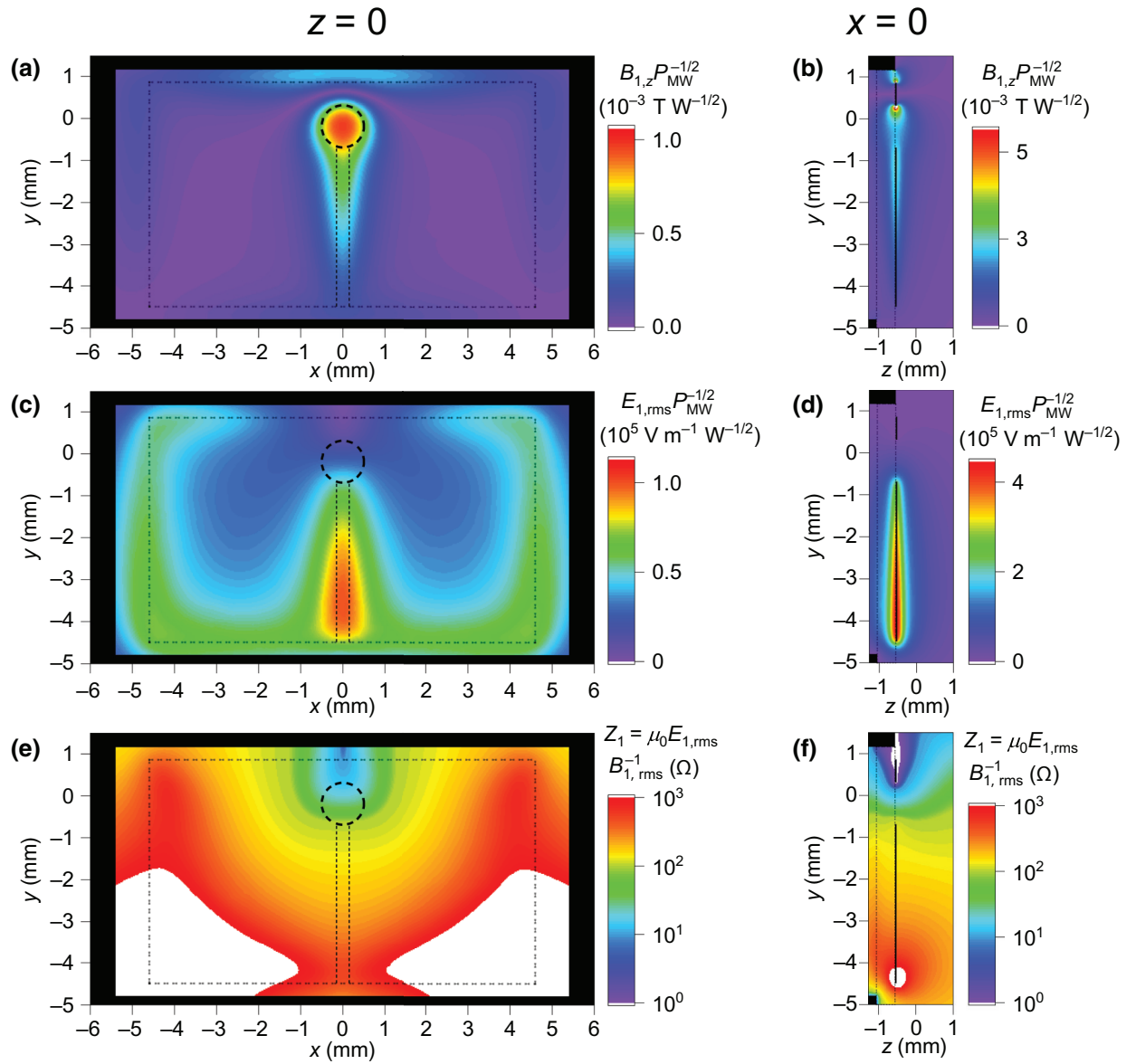
FIG. 5.   Calculated distribution of the microwave fields in the KHR-1 structure under resonant conditions. (a),(b) Amplitude of the z component of the magnetic field $B_{1,z}$. In (b) the same color scale corresponds to a wider range of field magnitudes. (c),(d) Root-mean-square amplitude of the electric field $E_{1,\mathrm{rms}}$. (e),(f) Impedance parameter $Z_1 = \mu_0 E_{1,\mathrm{rms}}/B_{1,\mathrm{rms}}$. The distributions in the x-y plane at $z = 0$ are shown in (a),(c),(e), with the dashed lines highlighting the contours of the metallization of the KHR, and the contours of the resonator shield shown by the black areas. The distributions in the y-z plane at $x = 0$ are shown in (b),(d),(f), with the solid (dashed) lines highlighting the contours of the metallization (PTFE substrate) of the KHR, whereas the contours of the resonator shield are shown by the black areas. See Figs. 1(a) and 1(b) for a representative three-dimensional view and orientation of the coordinate axes.

($z = 0$), located 0.52 mm from the KHR surface, the magnetic field is more uniform than at the KHR surface, and peaks closer to the axis of the circle at $y \approx -0.19$ mm, $z \approx 0$ mm, as can be seen in Fig. 5(a). It follows from Figs. 5(c) and 5(d) that the electric field of the resonant mode is maximum in the gap and is concentrated in the lower (negative-y) part of KHR gap, away from the loop. The peak rms electric field in the gap (in the $x = 0$ plane) is $E_{1,\mathrm{rms}} \approx 4.8 \times 10^5$ V m^{-1} W$^{-1/2}$. The resulting impedance

parameter $Z_1 = \mu_0 E_{1,\mathrm{rms}}/B_{1,\mathrm{rms}}$ shown in Figs. 5(e) and 5(f) decreases as one goes from the bottom of the gap (negative y) to the KHR circle and the top of the KHR (positive y). These results explain the advantage of the KHR profile—the long gap helps to separate the magnetic and electric fields of the mode, effectively focusing the magnetic component near the circle of the KHR and shifting the electric component away from the circle and toward the outer edge of the structure.

III. EXPERIMENTAL MICROWAVE REFLECTOMETRY AND PULSED ELECTRON SPIN RESONANCE ON SiC

A. Experimental setup

The validity of the design and simulations is verified in experiments, including microwave reflectometry to investigate the resonant modes and coherent ESR to evaluate the amplitude of the microwave magnetic field produced by the KHR. For these experiments a series of KHR structures are fabricated on a PTFE-based substrate (thickness 0.8 mm, Rogers laminate AD255C, dielectric constant $\varepsilon \approx 2.55$, dissipation factor 0.0013 at 10 GHz). The metallization thickness is 35 μm (copper) with an immersion silver finish.

The schematic of the entire experimental setup is shown in Fig. 6. A confocal optical microphotoluminescence setup is used. The light emitted by a 10-mW diode laser at 780 nm (Edmund Optics PGL-780-10mW+TTL) passes through a short-pass filter (Thorlabs FES0800) and is reflected by a dichroic mirror (Thorlabs DMLP805) to be focused by an aspheric objective lens (Thorlabs C390TME-B, focal length $F = 2.75$ mm, NA 0.55, effective working distance L_{opt}=1.91 mm) on the surface of a SiC sample. The photoluminescence (PL) is collected by the same objective and is sent through the dichroic mirror and two long-pass filters (Thorlabs FEL0800 and RazorEdge 830 nm) to another aspheric objective (Thorlabs C280TME-B), which focuses light into a single-mode fiber. The collected light is sent to an avalanche-photodiode (APD) single-photon counter (Excelitas SPCM-AQRH-14-FC). The use of a single-mode fiber (as opposed to a multimode fiber) provides additional spatial filtering of the collected light, ensuring the microwave field can be probed selectively in a volume with a few micron diameter. A static magnetic field B_0 is applied along the x axis. In this way, B_0 is perpendicular to the y direction, which is both the optical excitation axis and the c axis of the SiC crystal. The static field is produced by four permanent magnets (e-Magnets UK EP299N52, $25 \times 10 \times 5$ mm^3, N52 grade), with a stack of two magnets on each side of the sample to improve field homogeneity (not shown in Fig. 6). The magnet stacks can be moved to adjust the field, with one of the stacks attached to a computer-controlled actuator, providing field control with a relative accuracy of 0.01%.

The photon-counting pulses from the APD are routed through a switch (Minicircuits ZASWA-2-50DR+) into two pulse counters (TTi TF930). In ODMR experiments the switch and the microwave source gate are toggled every other measurement cycle so that the two counters accumulate the ODMR and the reference PL signals, which are then used to derive the microwave-induced relative change in PL signal. A typical collected PL signal from
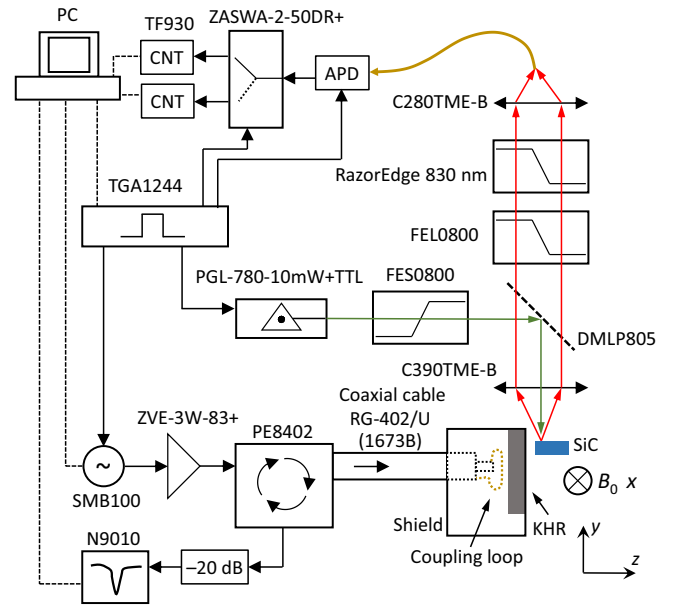

FIG. 6. The experimental setup used for microwave reflectometry and ODMR experiments. See the description in the main text. CNT, counter; PC personal computer.

the sample studied is approximately 4×10^6 photons per second under 10-mW laser excitation.

The assembly with a shield and a KHR is mounted next to the SiC sample to produce a microwave magnetic field along the z axis. The KHR is excited by a coupling coil wound with a 0.3-mm copper wire into a single loop of an approximately circular shape with a diameter of 6 mm. The coupling loop is fed through a coaxial cable (RG-402/U, conformable type 1673B) connected to the output of the circulator (Pasternack PE8402). The input of the circulator is fed by a microwave generator (Rohde&Schwarz SMB100) through an amplifier (Minicircuits ZVE-3W-83+), while the third port of the circulator is used to monitor the reflected microwave power on a spectrum analyzer (Agilent N9010).

Finally, a four-channel pulse generator (TTi TGA1244) is used for pulse modulation of the microwave and laser sources as well as for gating the APD and switching the APD pulses between the two counters to achieve differential measurement and perform pulsed magnetic resonance when required. The microwave source and the pulse generator are computer controlled; combined with computerized readout of the pulse counter and spectrum analyzer signals, this allows fully automated measurements.

B. Microwave reflectometry

The initial microwave-reflectometry experiments are conducted without any optical excitation or static magnetic field and consist of varying the distance between the coupling loop and the KHR to achieve critical coupling. Figure

4(a) shows the spectrum of the microwave power reflection coefficient S_{11} for the KHR-1 structure (thick solid line). A single absorption dip is observed at $f_r \approx 6.5865$ GHz, which is somewhat lower than the resonant frequency of 7.543 GHz predicted in numerical simulations (dashed line). The difference can be ascribed to the larger dielectric constant $\varepsilon \approx 2.55$ of the substrate compared with the pure PTFE ($\varepsilon \approx 2.03$) substrate used in simulations. The bandwidth of the measured resonance at the -3-dB power level is approximately 65 MHz, corresponding to the loaded quality factor $Q_L \approx 100$, from which the unloaded (intrinsic) Q factor $Q = 2Q_L \approx 200$ is derived. This is approximately 2 times smaller than the predicted Q_L of approximately 261, indicating additional losses not accounted for in the numerical simulations. The simulations indicate that resistive losses in the KHR metallization are the main source of energy dissipation—the discrepancy with experiment suggests additional losses due to imperfection (roughness or oxidation) of the metal surface. The small Q factors (large bandwidth) found in KHR structures are beneficial in coherent control experiments, where microwave pulses as short as a few tens of nanoseconds are required.

C. Optically detected magnetic resonance

To verify that the observed microwave resonance corresponds to the predicted subwavelength resonant mode, optically-detected-electron-spin-resonance experiments are conducted. The sample used is a semi-insulating and unprocessed wafer of 4H-SiC from Cree. The sample thickness is 0.35 mm and the surface orientation is {0001}. A typical room-temperature PL spectrum is shown in Fig. 7(a). ODMR is measured by application of cw optical excitation and detection of the difference in the integrated PL intensity with and without continuous-wave microwave excitation. In the absence of a static magnetic field, an ODMR spectrum is observed at $2D \approx 70$ MHz, while with a sufficiently large magnetic field perpendicular to the sample surface and parallel to the sample c axis (y axis of the laboratory frame, Faraday geometry) a doublet of ODMR lines with splitting $4D \approx 140$ MHz is observed. These spectral features are indicative of ODMR of single silicon vacancies in 4H-SiC, where D characterizes the crystal-field splitting of the spin-3/2 electron ground state [8,46,47]. The setup permits both Faraday and Voight configurations. However, when small permanent magnets are
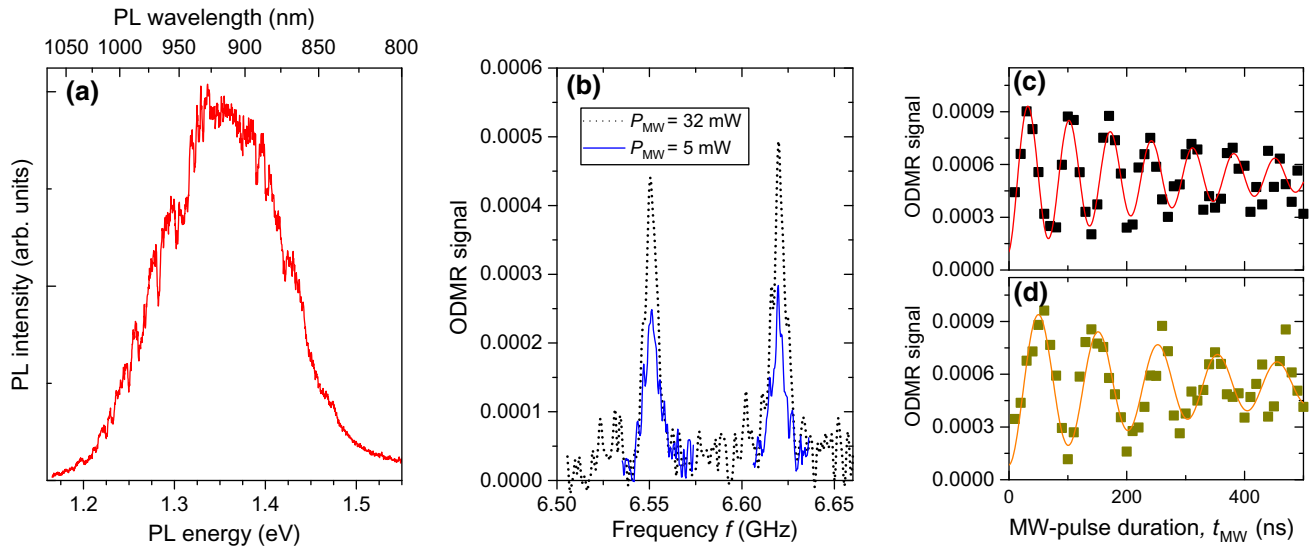

FIG. 7. (a) Room-temperature PL spectrum of a SiC sample measured at zero magnetic field under 561-nm laser excitation. (b) ODMR spectrum of an ensemble of silicon vacancies in SiC at room temperature measured under cw optical and microwave excitation at microwave powers P_{MW} of approximately 32 mW and approximately 5 mW. A static magnetic field is applied in the Voigt geometry and is orthogonal to the c axis of SiC. Optical excitation wavelength and power are approximately 760 nm and approximately 10 mW, respectively. ODMR signal is measured as a MW-induced relative change in PL intensity. (c) Rabi oscillations of the electron spins in silicon vacancies measured with the protocol (optical pump)–(microwave pulse)–(optical probe). Experimental results are shown by the symbols, whereas fitting is shown by the solid line, yielding a Rabi period T_{Rabi} of approximately 70 ns. The duration of the optical pump polarizing the electron spin is 50 μs, and the duration of the probe is 10 μs, of which the initial 4 μs is used to detect the spin polarization of the electron left after the microwave pulse of variable duration t_{MW}. The rms power of the microwave pulse is approximately 0.97 W. The magnetic field is adjusted so that the low-frequency ESR peak coincides with the microwave frequency $f = 6.5865$ GHz, which also matches the minimum-reflection frequency of the resonator. Optical excitation is the same as in (b). (d) Rabi oscillations of the electron spins located at a longer distance from the resonator, which results in reduced microwave-field amplitude and longer Rabi period, $T_{Rabi} \approx 100$ ns.

used, it is more convenient to work in the Voigt geometry, where the static magnetic field is oriented perpendicular to the c axis of the sample (along the x axis of the laboratory frame) since it is easier to achieve homogeneity of the static field. The static field is then tuned to have the SiC electron-spin-resonance frequency match the KHR resonance at $f_r \approx 6.5865$ GHz—the resulting cw ODMR spectra in the Voigt geometry at different microwave powers are shown in Fig. 7(b) and reveal a doublet with a full-width-at-half-maximum linewidth of 8 MHz and a splitting of $2D \approx 70$ MHz.

For pulsed ODMR measurements the static magnetic field is fine-tuned to match the low-frequency ODMR doublet component with the resonance of KHR-1 at $f_r \approx 6.5865$ GHz. The experimental cycle is similar to that used in previous work [46,47] and consists of a pump laser pulse to polarize the electron spins, followed by a microwave pulse in the dark, and finally a probe laser pulse during which the PL intensity is measured. The focused laser spot on the sample is only few micrometers in size (limited by diffraction), ensuring excellent spatial resolution in local probing of the microwave magnetic field. The KHR is positioned so that the laser spot on the sample corresponds approximately to $x = y = 0$ (i.e., shifted from the axis of the KHR circle by approximately 0.19 mm in the positive y direction) and the distance between the KHR and the laser spot in the z direction can be adjusted to probe the microwave field in different areas.

The symbols in Fig. 7(c) show the ODMR signal as a function of the duration of the microwave pulse t_{MW}. The pulse rms microwave power is $P_{MW} \approx 0.97$ W at the feeding loop and the microwaves are resonant with the low-frequency peak of the SiC ESR doublet. The laser and PL sampling spot is $L_{MW} \approx 0.57$ mm from the KHR surface, corresponding to the spot position $(x, y, z) = (0, 0, 0.05)$ mm. Clear oscillations with period $T_{Rabi} \approx 70$ ns are observed as revealed by fitting (line). On the basis of good agreement with previous work [46,47], we attribute these to coherent spin rotations. From these Rabi oscillations the amplitude of the microwave magnetic field B_1 is evaluated. The Rabi frequency is $1/T_{Rabi} = g_e \mu_B B_1/(2h)$, where μ_B is the Bohr magneton, $g_e \approx 2.0$ is the electron g factor, h is the Plank constant, and the additional factor $1/2$ is used to convert the laboratory-frame field amplitude B_1 to the amplitude $B_1/2$ of the component acting on the spins in the rotating frame. From this the field is derived to be $B_1 \approx 1.02$ mT, and the conversion factor is $B_1 P_{MW}^{-1/2} \approx 1.04 \times 10^{-3}$ T W$^{-1/2}$, or $1/(T_{Rabi} P_{MW}^{1/2}) \approx 14.5$ MHz W$^{-1/2}$ in terms of the Rabi frequency.

A further measurement [Fig. 7(d)] is conducted by our shifting the laser and PL spot to a longer distance of $L_{MW} \approx 0.7$ mm from the KHR surface, which is seen to result in a reduced oscillation frequency. While the MW-power dependence is not studied here directly, this observation supports the interpretation that the oscillations are due to the coherent Rabi spin rotations. The smaller microwave field $B_1 P_{MW}^{-1/2} \approx 0.71 \times 10^{-3}$ T W$^{-1/2}$ derived at larger $L_{MW} \approx 0.7$ mm confirms that the microwave magnetic field is highly localized and arises from the resonant mode of the KHR predicted in simulations (Fig. 5). Both measurements are shown by the triangles in Fig. 4(c) and agree with the simulations for KHR-1 (dashed line). The somewhat higher experimental values are likely due to the effect of the $B_{1,y}$ component, which contributes to spin resonance for the static magnetic field along the x axis. Accurate profiling of the spatial field distribution is limited by the microwave power P_{MW} available for this work: higher P_{MW} would be needed at a long distance from the resonator to achieve a Rabi frequency that exceeds ESR broadening and would allow Rabi oscillations to be observed clearly. Examination of the field very close to the KHR metallization is complicated as well, since optical access to the sample point becomes restricted.

The experimental conversion efficiency $B_1 P_{MW}^{-1/2} \approx 1.04 \times 10^{-3}$ T W$^{-1/2}$ of KHR-1 can be compared with that obtained in previous ODMR studies on quantum defects such as nitrogen vacancies in diamond. Similar conversion efficiency of approximately 1.5×10^{-3} T W$^{-1/2}$ was reported [48] but at lower frequency of approximately 3 GHz and with use of very close proximity to a feeding wire $L_{MW} \approx 0.01$–0.02 mm. For a lower frequency of approximately 0.4 GHz, an even higher $B_1 P_{MW}^{-1/2}$ of approximately 4.6×10^{-3} T W$^{-1/2}$ was reported with a coplanar waveguide fabricated on the sample surface [49]. By contrast, for a sample mounted on a miniaturized loop [50], the conversion factor was lower ($B_1 P_{MW}^{-1/2} \approx 0.27 \times 10^{-3}$ T W$^{-1/2}$) at approximately 3 GHz. This comparison confirms that the KHR design offers optical access and high microwave power-to-field conversion, while providing a long microwave working distance, thus avoiding the need for direct contact with the sample or additional sample fabrication. These properties are beneficial when reduction of parasitic microwave electric fields is important.

With the bandwidth of approximately 65 MHz measured for KHR-1, it is possible to achieve microwave pulses as short as approximately 20 ns. On the basis of the measured conversion factor $B_1 P_{MW}^{-1/2}$, a π-rotation pulse of such duration can be achieved at a microwave power P_{MW} of approximately 3 W for a sample with $g_e \approx 2.0$. In semiconductor structures, where electron g factors are smaller, higher power would be required: for example, for $|g_e| \approx 0.2$ found in GaAs, a π rotation with a duration of $t_{MW} \approx 20$ ns would require $P_{MW} \approx 300$ W, which can be achieved with a conventional solid-state or traveling-wave tube amplifier.

IV. EFFECT OF KHR PARAMETERS ON RESONANT MODES

The KHR-1 design is used as a starting point to investigate the effect of the geometry on the resonant modes of the KHR. The effect of the KHR dimensions on the resonant frequency derived from numerical simulations (solid symbols) is demonstrated in Fig. 8. The increase of the area of the KHR metal layer results in reduction of the resonance frequency, both when the width of the structure w [Fig. 8(a)] and when the length of the gap l
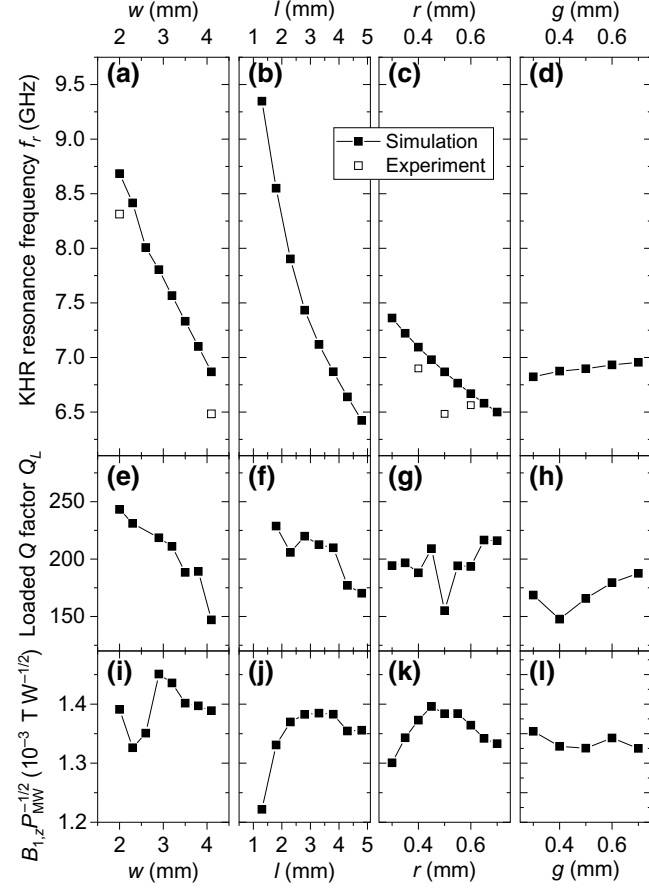

FIG. 8. KHR resonance-mode parameters derived from numerical simulations (solid symbols) as a function of the KHR structural parameters [see the drawing in Fig. 1(d)]. (a)–(d) The resonance frequency. (a) w is varied while $r = 0.5$ mm, $l = 3.8$ mm, and $g = 0.3$ mm are kept constant. (b) l is varied while $r = 0.5$ mm, $w = 4.1$ mm, and $g = 0.3$ mm are kept constant. (c) r is varied while $g = 0.3$ mm is kept constant and the overall footprint of metallization is maintained by the adjustments $w = 4.1 - (r - 0.5)$ mm and $l = 3.8 - 2(r - 0.5)$ mm. (d) g is changed while $r = 0.5$ mm, $w = 4.1$ mm, and $l = 3.8$ mm are kept constant. In all designs, $m_t = 0.3$ mm. Open symbols show the measured resonance frequencies for those structures that are examined experimentally. (e)–(h) Loaded Q factor Q_L under critical coupling. (i)–(l) Microwave-magnetic-field conversion factor $B_{1,z}P_{MW}^{-1/2}$ at the sample point $(x, y, z) = (0, 0, 0)$.

[Fig. 8(b)] are increased. The increase of the KHR circle radius r [Fig. 8(c)] and the reduction of the gap g [Fig. 8(d)] also reduce the resonance frequency, but the changes are less pronounced. These observations suggest that in contrast to LGRs, where the loop and the gap are predominantly responsible for inductance and capacitance, respectively, in the KHR both are distributed across the structure. The resonance frequency of the structure can be designed by altering the overall area of the KHR rectangular footprint. The possibility of achieving a low resonance frequency even with a large gap g could be beneficial in high-power applications, where concentration of the electric field across a small gap can result in undesired dielectric breakdown and arcing. Experimental resonant frequencies obtained from microwave reflectometry for several structures are shown by the open symbols and are in good agreement with simulations, confirming the trends in parametric dependencies.

When the KHR geometry is varied, the Q factors are found to be similar within computational error [Figs. 8(e)–8(h)], except that smaller w [Fig. 8(e)] tends to give higher Q_L. Equally, the peak microwave-magnetic-field amplitude is found to be constant within approximately 20% under all parameter variations [Figs. 8(i)–8(l)].

V. FURTHER DEVELOPMENT OF KHR DESIGNS

Having described the development of and experimental tests on KHR structures, we explore potential design improvements. First, the possibility of further suppression of the microwave electric field is examined. To this end, bridged-KHR (BKHR) structures are explored, where similarly to BLGRs, an additional metal layer is introduced to contain the electric field within a limited volume. The structure is a modification of the KHR shown in Fig. 1(d). First, a spacer layer of PTFE with a rectangular footprint is added on top of the KHR metallization layer—the rectangular footprint is of length l in the y direction matching the gap, and of width $2g$ along the x direction, centered at $x = 0$, thus covering the gap g of the KHR with an overlap. Then a bridge layer of copper of the same footprint is added on top of this PTFE spacer. This way the bridge shields the sample area $z > -L_{MW}$ from stray electric fields. Similarly to the KHR, such structures can be produced by standard fabrication techniques on multilayer PCBs. The optimization is repeated by variation of the same structural parameters c, w, l, g, r, m_t, and m_h as in the case of the KHR, and the resulting Pareto front is shown in Fig. 3 by the solid squares. The BKHR gives a very similar maximum microwave magnetic field $B_{1,z}P_{MW}^{-1/2}$, but with a considerably reduced electric field (smaller Z_1) at the sample point, confirming that the electric component of the mode can be contained further by addition of a bridge. The optimal BKHR geometry at $f_0 = 7.5$ GHz corresponds to $c = 0.36$ mm, $w = 2.0$ mm, $l = 4.5$ mm, $g = 0.6$ mm,

$r = 0.51$ mm, $m_t = 0.35$ mm, and $m_h = 4.0$ mm, similar to the KHR without the bridge.

Next, a dual-BKHR design with improved microwave-field homogeneity is considered. This design is achieved by addition of a mirror copy of the BKHR with its shield, the feeding cable, and the coupling loop. The mirror plane is $z = 0$, so the circles of the two BKHR structures have a common axis, and both resonators are excited simultaneously by application of the same microwave signal in phase to the two coupling loops. The geometry of the two BKHRs is optimized at $f_0 = 7.5$ GHz and $L_{MW} = 0.52$ mm. The resulting Pareto optimal front is shown by the stars in Fig. 3, demonstrating that the dual-BKHR design outperforms both the single-KHR design and the single-BKHR design: the conversion factor $B_{1,z}P_{MW}^{-1/2}$ for the sample point $(x, y, z) = (0, 0, 0)$ can be as large as approximately 1.45×10^{-3} T W$^{-1/2}$ and is achieved at $Z_1 \approx 35$ Ω, similarly to other KHR structures. The largest conversion factor is achieved at $c = 0.35$ mm, $w = 2.2$ mm, $l = 4.2$ mm, $g = 0.47$ mm, $r = 0.54$ mm, $m_t = 0.3$ mm, and $m_h = 2.8$ mm. To move along the Pareto front, the parameters can be changed to $c = 0.55$ mm, $w = 1.0$ mm, $l = 6.3$ mm, $g = 0.8$ mm, $r = 0.2$ mm, $m_t = 0.2$ mm, and $m_h = 5.2$ mm, in which case the circle becomes smaller than the gap width and the KHR design essentially becomes a bridged slot resembling the U-shaped surface LGR design studied previously [31]. Such a modified design provides a factor-of-5 reduction in the relative electric field ($Z_1 \approx 7$ Ω) while sacrificing 35% in conversion factor (reduction down to $B_{1,z}P_{MW}^{-1/2} \approx 1.07 \times 10^{-3}$ T $\times$ W$^{-1/2}$).

Importantly, the dual-BKHR design significantly improves homogeneity of the microwave magnetic field. Since many solid-state spin-qubit structures have planar designs, homogeneity is evaluated in the optical focal plane $y = 0$, rather than over a volume. Figure 9 shows the distribution of the microwave field $B_{1,z}$ in the $y = 0$ plane for the KHR-1 design considered previously [Fig. 9(a)] and for the optimized dual-BKHR structure [Fig. 9(b)] with the same microwave working distance $L_{MW} = 0.52$ mm. The solid black lines show the contours of the areas where $B_{1,z}$ deviates by less than $\pm20\%$ from the value at the sample point $(x, y, z) = (0, 0, 0)$. For a single KHR, the area of homogeneous $B_{1,z}$ is approximately 0.21 mm^2 and forms a narrow crescent. By contrast, the dual-BKHR design provides a large area (approximately 0.6 mm^2) of homogeneous $B_{1,z}$ filling nearly the entire gap between the two opposing BKHRs. A further comparison is presented in Fig. 4(c), where $B_{1,z}$ along the z direction at $x = y = 0$ is shown for the dual-BKHR design by the solid line. Figure 9 shows that KHR structures act similarly to a near-field subwavelength lens [51–56], focusing $\lambda \approx 4$ cm electromagnetic waves into a submilliliter free-space volume.

It is worth noting that the improvement in $B_{1,z}$ and its homogeneity in the dual-BKHR design comes at the
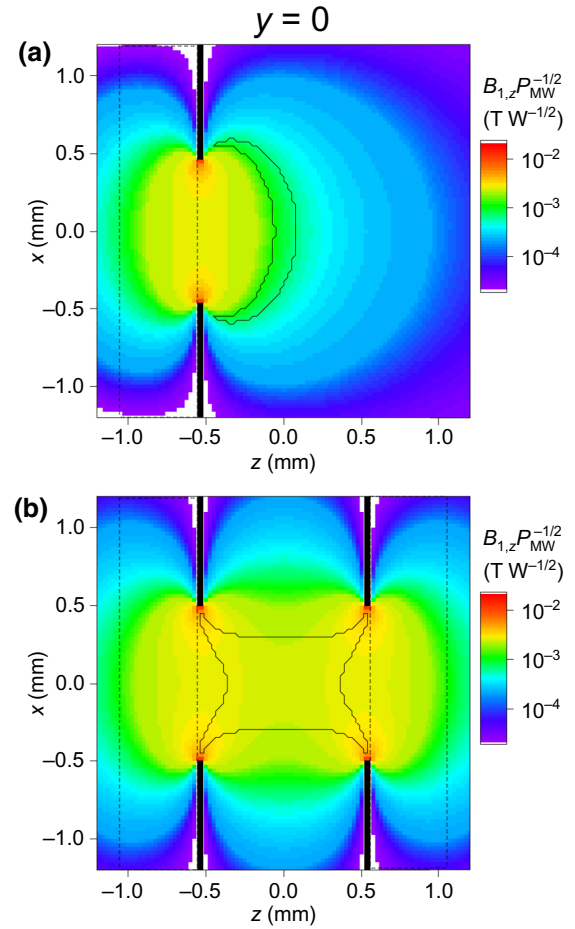

$y = 0$

FIG. 9. Calculated distribution of the microwave magnetic field $B_{1,z}$ in KHR-1 (a) and the dual-BKHR design (b) under resonant conditions. The distributions are shown in the x-z plane at $y = 0$, with the dashed lines highlighting the contours of the PTFE substrates, and the black areas showing the metallization of the KHR. Solid black contour lines show the areas of a homogeneous microwave field where $B_{1,z}$ deviates from $B_{1,z}$ at the sample point $(x, y, z) = (0, 0, 0)$ by no more than $\pm20\%$.

expense of the optical collection efficiency, since BKHRs and their shields obstruct some of the optical rays. To examine this relation, an objective with a NA of 0.55 is considered, as used in the experiments reported in Sec. III. After the shadow from a single KHR or BKHR [the design shown in Figs. 1(a) and 1(b)] is taken into account, the effective numerical aperture is calculated to be approximately 0.47, while in the dual-BKHR configuration it is reduced to approximately 0.36, which is still suitable for efficient optical collection. Alternatively, the optical collection efficiency can be improved with use of an objective that is small enough to fit between the BKHRs, or by the use of a solid immersion lens, which would effectively provide the same optical collection efficiency as without any microwave structures.

VI. DISCUSSION AND OUTLOOK

In conclusion, a series of microwave-resonator structures with a keyhole profile are studied in numerical simulations and ODMR experiments. The structures are designed with the aim of simultaneous focusing of optical and microwave fields given finite constraints on the minimum working distance between the sample and the microwave-resonator elements. Systematic multiobjective optimization is used to find the best combination of resonator geometrical parameters that maximize the microwave-magnetic-field conversion factor while minimizing the microwave electric field. The resonator structures are cheap and easy to manufacture by standard printed-circuit-board fabrication methods. Unlike the conventional bulk and surface LGRs, the KHR assembly supports optical excitation along the axis orthogonal to the microwave magnetic field, which is demonstrated experimentally with use of fast coherent manipulation of a small ensemble of the defect electron spins in SiC. The resonators are naturally suited for optically detected magnetic resonance of individual quantum objects, including semiconductor defects and quantum dots. This can be achieved through optical resolution of low-density individual spins. In those applications in quantum sensing and computing where it is necessary to control multiple closely spaced (less than the optical wavelength) individual spins, resolution can be achieved by shifting the resonance frequencies through nanoscale magnetic field gradients [57,58]—in such scenarios, KHRs are advantageous as they offer a large resonance bandwidth to control multiple individual qubits.

Future work will include improvement in microwave-focusing performance by means of further miniaturization, more-complex shapes, and multilayer metal-dielectric structures. Concentration of microwave fields at micron and submicron scales would be a challenging goal, achieving which would allow selective control in nanoscale multiqubit ensembles—in this case the millimeter-sized KHRs examined here can act as a first-stage contactless feeder for smaller resonating structures of the subsequent focusing stages. Moreover, the structures can be optimized for additional or alternative objectives, such as resonator bandwidth or spatial homogeneity of the microwave magnetic field.

ACKNOWLEDGMENTS

APPENDIX: DETAILS OF MICROWAVE STRUCTURE MODELING

This appendix describes an example of the code used to simulate the microwave response of the KHR structures, which is included as Supplemental Material [42]. The model relies on freely available software.

The first step in the simulation is to define the geometry of the structure and generate a tetrahedral mesh approximating the model. This is done with Gmsh 4.6.0 [59], with use of OPEN CASCADE TECHNOLOGY. An example meshed structure can be found in the file KHR-1.msh, and can be opened in Gmsh for inspection. A screenshot of a meshed geometry from Gmsh is shown in Fig. 10(a). The geometry of the model is enclosed in a rectangular bounding box with approximate dimensions $16.0 \times 9.5 \times 5.0$ mm^3 along the x, y and z axes, respectively. The geometry is similar to that of KHR-1 shown in Figs. 1(a) and 1(b), including the KHR substrate and metallization, metal resonator shield, and a ring-shaped torus of revolution approximating the coupling loop. The minor radius of the torus (wire radius) is 0.3 mm, and the major radius (of the revolution circle) is 1.3 mm. At high frequencies only the surfaces of the metal objects conduct electric currents (approximation of infinitely small skin depth). Therefore, the coupling loop torus, KHR metallization, and resonator shield are approximated as hollow volumes (with use of the "BooleanDifference" operator in Gmsh). By contrast, the PTFE substrate of the KHR is modeled as a solid parallelepiped (with use of the "BooleanFragments" operator in Gmsh).

Once the geometry is defined and meshed, the discretized time-harmonic Maxwell equation and the boundary conditions are defined. This is done with the "Vectorial Helmholtz" solver model in the finite-element-method program ELMER 9.0 [60]. Figure 10(b) shows a screenshot of a meshed geometry viewed in ElmerGUI. The volume of the structure is modeled as air with close-to-unity dielectric constant $\epsilon \approx 1$, while the KHR substrate is modeled as lossy PTFE with $\epsilon \approx 2.03 + 0.000\,812i$. The surfaces of the bounding box and the resonator shield are modeled as perfect electric conductors, by setting the boundary condition $\vec{E} \times \vec{n} = \vec{0}$, which imposes a zero tangential component of the electric field $\vec{E}$. The surfaces of the KHR metallization are modeled with the Leontovich impedance boundary condition [61], using silver conductivity $\sigma \approx 6.3 \times 10^7$ S m^{-1}. Finally, the electromagnetic field is excited in the model by setting Dirichlet boundary conditions for the electric field on the surface of the torus, which provides a simplified approximation for a real coupling loop connected to a coaxial cable. The axis of revolution of the torus is aligned with the z axis, and the components of the electric field are set to be $E_x = (y - y_0)/[2\pi(x - x_0)^2 + 2\pi(y - y_0)^2]$ and $E_y = -(x - x_0)/[2\pi(x - x_0)^2 + 2\pi(y - y_0)^2]$, where x_0 and y_0 are the coordinates of the torus axis. Such a boundary
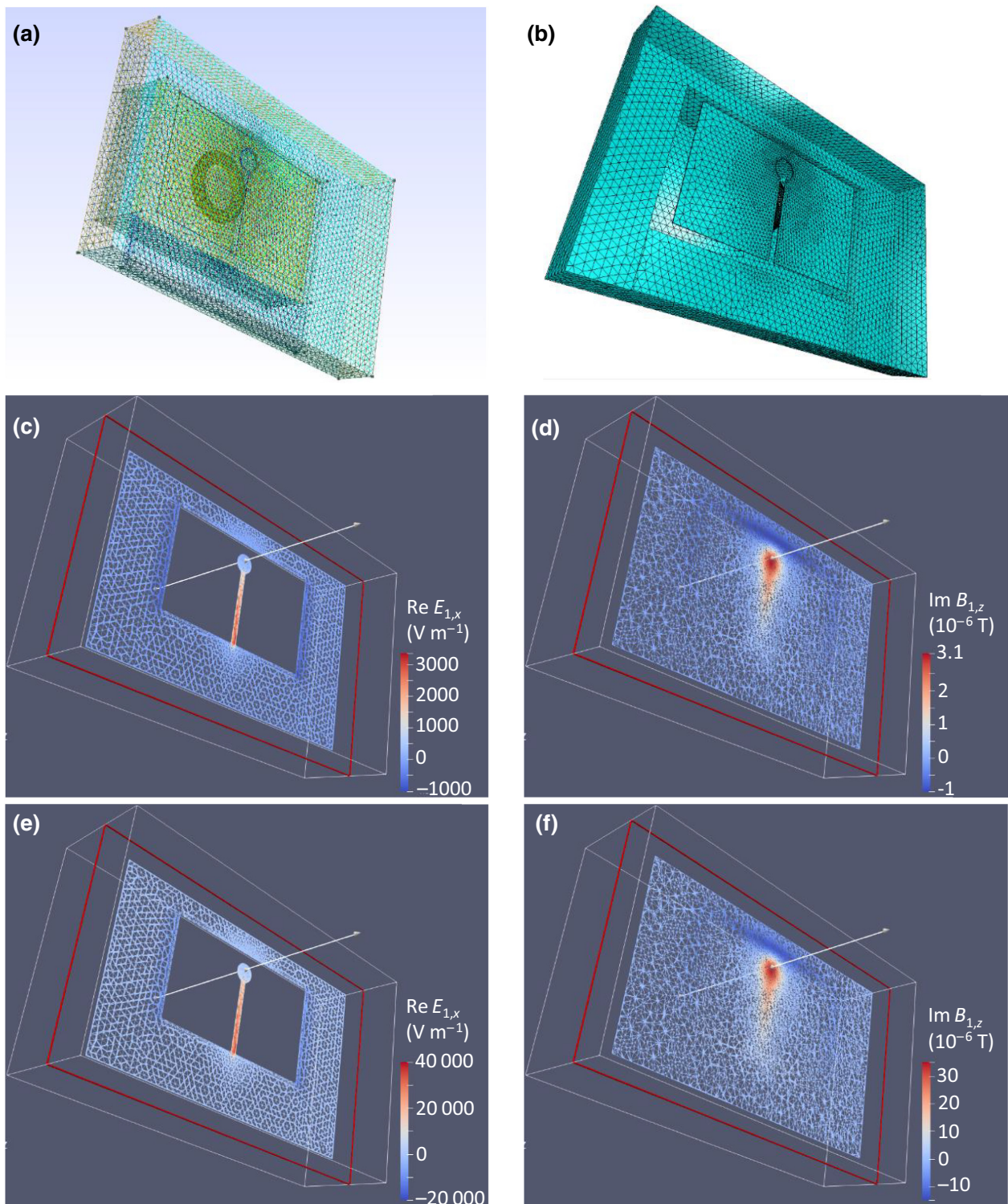
FIG. 10.   (a) Tetrahedral mesh generated and visualized with Gmsh for a model consisting of a KHR, a resonator shield, and a feeding loop. (b) Same model visualized in ElmerGUI. Some of the model surfaces are hidden to allow the internal elements to be seen. (c) Real part of the complex amplitude of the electric field component $E_{1,x}$. The plot is for excitation frequency $f = 7.0$ GHz and for a plane $z = -0.52$ mm that matches the plane of KHR metallization. (d) Imaginary part of the complex amplitude of the magnetic field component $B_{1,z}$. The plot is for excitation frequency $f = 7.0$ GHz and for a plane $z = 0$ mm. (e) Same as (c) but at $f = 7.36$ GHz. (f) Same as (d) but at $f = 7.36$ GHz.

condition defines a circulating electric field with a unity voltage (1 V) on the coupling loop.

The Maxwell equation is then solved with the biconjugate-gradient stabilized method with polynomial order 10, and the spatial distribution of the complex amplitudes of electric and magnetic fields is derived. The field values at the mesh nodes are stored in files named `case_t0001.vtu`. The spatial configurations of the fields can be inspected with ParaView 5.8.1, as exemplified in Figs. 10(c) and 10(e), which show screenshots of the electric field magnitude E_{1x} in the plane of the KHR metallization. Figures 10(d) and 10(f) show the magnetic field flux-density amplitudes B_{1z} in the $z = 0$ plane, which are similar to the field distribution shown in Fig. 5(a). The field amplitudes can be calculated at any location, including the sample point $(x, y, z) = (0, 0, 0)$. To derive normalized field amplitudes, as shown for the examples in Figs. 4(b) and 4(c) and 8(i)–8(l), the microwave power delivered through the feeding loop needs to be calculated. The voltage V on the coil is known, since it is given by the boundary conditions. The circular current I flowing in the toroidal direction (direction of revolution) of the feeding loop is calculated by integration of the magnetic field $\vec{B}$ over the poloidal direction (i.e., along the length of the minor-radius circle made by the cross section of the feeding-loop wire). The calculation uses Ampere's law for time-harmonic fields $1/\mu_0 \oint_{\partial\Sigma} \vec{B} \cdot d\vec{l} = \iint_\Sigma \vec{J} \cdot d\vec{S} + i\omega\epsilon\epsilon_0 \iint_\Sigma \vec{E} \cdot d\vec{S}$, taking into account that the torus is hollow, thus rendering the last surface integral of the electric field $\vec{E}$ to be zero. Because of the infinitely small skin depth, the volume current density $\vec{J}$ is a δ function of the wire cross-section radius, so the first integral on the right side of the equation gives the total surface-current complex amplitude $I = \iint_\Sigma \vec{J} \cdot d\vec{S} = 1/\mu_0 \oint_{\partial\Sigma} \vec{B} \cdot d\vec{l}$. The microwave power P_{MW} of a source with internal impedance $Z_0 = 50$ Ω that would be required to produce such a voltage V and current I is calculated as $P_{MW} = |IZ_0 + V|^2/(4Z_0)$, and is used to normalize all the derived field values. The complex impedance V/I of the coupling loop is then used to calculate the scattering parameter $S_{11} = 10\log_{10}(1 - \text{Re}\{4Z_0(V/I)|1/[Z_0 + (V/I)]|^2\})$, which characterizes the power reflection shown, for example, in Fig. 4(a).

The Supplemental Material [42] includes calculated examples for two different excitation frequencies, 7.0 and 7.36 GHz, with results placed in the corresponding subfolders. At $f = 7.0$ GHz the microwave structure is off resonance, resulting in weak excitation of the KHR mode [Figs. 10(c) and 10(d)]. By contrast, at $f = 7.36$ GHz, excitation is close to resonance, resulting in significantly increased amplitudes of the electric and magnetic fields [Figs. 10(e) and 10(f)]. Under such near-resonance excitation the impedance presented by the feeding loop coupled inductively to the KHR is found to be 52.19 −

10.72i Ω, resulting in good impedance matching to a 50-Ω microwave source. For off-resonant excitation ($f = 7.0$ GHz), the impedance is almost purely imaginary, 22.69 − 1735.56i Ω, resulting in strong reflection of the microwave power. In general, when the distance between the feeding loop and the KHR is decreased (increased), the change of magnetic flux linkage results in a smaller (larger) real part of the on-resonance impedance. Thus, by adjustment of the microwave frequency and the coupling-loop position, it is possible to achieve matching to the impedance of the microwave source (50 Ω in the present work).

The mesh size in the examples in the Supplemental Material [42] is kept at approximately 36 000 nodes to get a compromise between accuracy and the size of the files with microwave-field distributions. The resulting resonant frequencies deviate by only approximately 2% from simulations on more-refined meshes [e.g., Fig. 4(a)]. Results with increased mesh resolution can be obtained by an adaptive mesh-refinement strategy, where one starts with a coarse mesh and then refines the areas where the solution error is large. Note that in the example code, the x and y axes are swapped compared with the notation used throughout the paper.

[1] W. Froncisz and J. S. Hyde, The loop-gap resonator: A new microwave lumped circuit ESR sample structure, J. Magn. Reson. (1969) **47**, 515 (1982).

[2] M. Mehdizadeh, T. K. Ishii, J. S. Hyde, and W. Froncisz, Loop-gap resonator: A lumped mode microwave resonant structure, IEEE Trans. Microw. Theory. Tech. **31**, 1059 (1983).

[3] R. Gallay and J. J. van der Klink, Resonator and coupling structure for spin-echo ESR, J. Phys. E: Sci. Instrum. **19**, 226 (1986).

[4] P. Neumann, I. Jakobi, F. Dolde, C. Burk, R. Reuter, G. Waldherr, J. Honert, T. Wolf, A. Brunner, J. H. Shim, D. Suter, H. Sumiya, J. Isoya, and J. Wrachtrup, High-precision nanoscale temperature sensing using single defects in diamond, Nano Lett. **13**, 2738 (2013).

[5] H. Kraus, V. A. Soltamov, F. Fuchs, D. Simin, A. Sperlich, P. G. Baranov, G. V. Astakhov, and V. Dyakonov, Magnetic field and temperature sensing with atomic-scale spin defects in silicon carbide, Sci. Rep. **4**, 5303 (2014).

[6] D. D. Awschalom, R. Hanson, J. Wrachtrup, and B. B. Zhou, Quantum technologies with optically interfaced solid-state spins, Nat. Photonics **12**, 516 (2018).

[7] M. Kroner, K. M. Weiss, B. Biedermann, S. Seidl, S. Manus, A. W. Holleitner, A. Badolato, P. M. Petroff, B. D. Gerardot, R. J. Warburton, and K. Karrai, Optical Detection of Single-Electron Spin Resonance in a Quantum Dot, Phys. Rev. Lett. **100**, 156803 (2008).

[8] D. J. Christle, A. L. Falk, P. Andrich, P. V. Klimov, J. U. Hassan, N. Son, E. Janzén, T. Ohshima, and D. D. Awschalom, Isolated electron spins in silicon carbide with millisecond coherence times, Nat. Mater. **14**, 160 (2015).

[9] E. A. Chekhovich, M. Hopkinson, M. S. Skolnick, and A. I. Tartakovskii, Suppression of nuclear spin bath fluctuations in self-assembled quantum dots induced by inhomogeneous strain, Nat. Commun. **6,** 6348 (2015).

[10] G. D. Fuchs, G. Burkard, P. V. Klimov, and D. D. Awschalom, A quantum memory intrinsic to single nitrogen–vacancy centres in diamond, Nat. Phys. **7,** 789 (2011).

[11] G. Wolfowicz, H. Maier-Flaig, R. Marino, A. Ferrier, H. Vezin, J. J. L. Morton, and P. Goldner, Coherent Storage of Microwave Excitations in Rare-Earth Nuclear Spins, Phys. Rev. Lett. **114,** 170503 (2015).

[12] M. V. G. Dutt, L. Childress, L. Jiang, E. Togan, J. Maze, F. Jelezko, A. S. Zibrov, P. R. Hemmer, and M. D. Lukin, Quantum register based on individual electronic and nuclear spin qubits in diamond, Science **316,** 1312 (2007).

[13] K. Saeedi, S. Simmons, J. Z. Salvail, P. Dluhy, H. Riemann, N. V. Abrosimov, P. Becker, H.-J. Pohl, J. J. L. Morton, and M. L. W. Thewalt, Room-temperature quantum bit storage exceeding 39 minutes using ionized donors in silicon-28, Science **342,** 830 (2013).

[14] A. M. Waeber, G. Gillard, G. Ragunathan, M. Hopkinson, P. Spencer, D. A. Ritchie, M. S. Skolnick, and E. A. Chekhovich, Pulse control protocols for preserving coherence in dipolar-coupled nuclear spin baths, Nat. Commun. **10,** 3157 (2019).

[15] M. Hirose and P. Cappellaro, Coherent feedback control of a single qubit in diamond, Nature **532,** 77 (2016).

[16] E. A. Chekhovich, S. F. C. da Silva, and A. Rastelli, Nuclear spin quantum register in an optically active semiconductor quantum dot, Nat. Nanotechnol. **15,** 999 (2020).

[17] B. Eble, O. Krebs, A. Lemaître, K. Kowalik, A. Kudelski, P. Voisin, B. Urbaszek, X. Marie, and T. Amand, Dynamic nuclear polarization of a single charge-tunable InAs/GaAs quantum dot, Phys. Rev. B **74,** 081306(R) (2006).

[18] M. Atatüre, J. Dreiser, A. Badolato, A. Högele, K. Karrai, and A. Imamoglu, Quantum-dot spin-state preparation with near-unity fidelity, Science **312,** 551 (2006).

[19] J. Puebla, E. A. Chekhovich, M. Hopkinson, P. Senellart, A. Lemaitre, M. S. Skolnick, and A. I. Tartakovskii, Dynamic nuclear polarization in InGaAs/GaAs and GaAs/AlGaAs quantum dots under nonresonant ultralow-power optical excitation, Phys. Rev. B **88,** 045306 (2013).

[20] V. Y. Ivanov, T. S. Shamirzaev, D. R. Yakovlev, A. K. Gutakovskii, L. Owczarczyk, and M. Bayer, Optically detected magnetic resonance of photoexcited electrons in (In, Al)As/AlAs quantum dots with indirect band gap and type-I band alignment, Phys. Rev. B **97,** 245306 (2018).

[21] I. Söllner, S. Mahmoodian, S. L. Hansen, L. Midolo, A. Javadi, G. Kirsanske, T. Pregnolato, H. El-Ella, E. H. Lee, J. D. Song, S. Stobbe, and P. Lodahl, Deterministic photon-emitter coupling in chiral photonic circuits, Nat. Nanotechnol. **10,** 775 (2015).

[22] A. M. Waeber, M. Hopkinson, I. Farrer, D. A. Ritchie, J. Nilsson, R. M. Stevenson, A. J. Bennett, A. J. Shields, G. Burkard, A. I. Tartakovskii, M. S. Skolnick, and E. A. Chekhovich, Few-second-long correlation times in a quantum dot nuclear spin bath probed by frequency-comb nuclear magnetic resonance spectroscopy, Nat. Phys. **12,** 688 (2016).

[23] R. J. Coles, D. M. Price, J. E. Dixon, B. Royall, E. Clarke, P. Kok, M. S. Skolnick, A. M. Fox, and M. N. Makhonin,

Chirality of nanophotonic waveguide with embedded quantum emitter for unidirectional spin transfer, Nat. Commun. **7,** 11183 (2016).

[24] G. Gillard, I. M. Griffiths, G. Ragunathan, A. Ulhaq, C. McEwan, E. Clarke, and E. A. Chekhovich, Fundamental limits of electron and nuclear spin qubit lifetimes in an isolated self-assembled quantum dot, npj Quantum Inf. **7,** 43 (2021).

[25] R. Narkowicz, H. Ogata, E. Reijerse, and D. Suter, A cryogenic receiver for EPR, J. Magn. Reson. **237,** 79 (2013).

[26] R. Narkowicz, D. Suter, and I. Niemeyer, Scaling of sensitivity and efficiency in planar microresonators for electron spin resonance, Rev. Sci. Instrum. **79,** 084702 (2008).

[27] P. Gay-Balmaz and O. J. F. Martin, Electromagnetic resonances in individual and coupled split-ring resonators, J. Appl. Phys. **92,** 2929 (2002).

[28] J. Garcia-Garcia, F. Martin, J. D. Baena, R. Marques, and L. Jelinek, On the resonances and polarizabilities of split ring resonators, J. Appl. Phys. **98,** 033103 (2005).

[29] K. Aydin and E. Ozbay, Identifying magnetic response of split-ring resonators at microwave frequencies, Opto-Electron. Rev. **14,** 193 (2006).

[30] F. Dolde, I. Jakobi, B. Naydenov, N. Zhao, S. Pezzagna, C. Trautmann, J. Meijer, P. Neumann, F. Jelezko, and J. Wrachtrup, Room-temperature entanglement between single defect spins in diamond, Nat. Phys. **9,** 139 (2013).

[31] Y. Twig, E. Suhovoy, and A. Blank, Sensitive surface loop-gap microresonators for electron spin resonance, Rev. Sci. Instrum. **81,** 104703 (2010).

[32] Y. Twig, E. Dikarov, W. D. Hutchison, and A. Blank, Note: High sensitivity pulsed electron spin resonance spectroscopy with induction detection, Rev. Sci. Instrum. **82,** 076105 (2011).

[33] Y. Twig, E. Dikarov, and A. Blank, Ultra miniature resonators for electron spin resonance: Sensitivity analysis, design and construction methods, and potential applications, Mol. Phys. **111,** 2674 (2013).

[34] N. Dayan, Y. Ishay, Y. Artzi, D. Cristea, E. Reijerse, P. Kuppusamy, and A. Blank, Advanced surface resonators for electron spin resonance of single microcrystals, Rev. Sci. Instrum. **89,** 124707 (2018).

[35] A. Bienfait, J. J. Pla, Y. Kubo, M. Stern, X. Zhou, C. C. Lo, C. D. Weis, T. Schenkel, M. L. W. Thewalt, D. Vion, D. Esteve, B. Julsgaard, K. Mølmer, J. J. L. Morton, and P. Bertet, Reaching the quantum limit of sensitivity in electron spin resonance, Nat. Nanotechnol. **11,** 253 (2016).

[36] S. Pfenninger, J. Forrer, A. Schweiger, and T. Weiland, Bridged loop-gap resonator: A resonant structure for pulsed ESR transparent to high-frequency radiation, Rev. Sci. Instrum. **59,** 752 (1988).

[37] M. Ono, T. Ogata, K.-C. Hsieh, M. Suzuki, E. Yoshida, and H. Kamada, L-band ESR spectrometer using a loop-gap resonator for in vivo analysis, Chem. Lett. **15,** 491 (1986).

[38] F. H. L. Koppens, C. Buizert, K. J. Tielrooij, I. T. Vink, K. C. Nowack, T. Meunier, L. P. Kouwenhoven, and L. M. K. Vandersypen, Driven coherent oscillations of a single electron spin in a quantum dot, Nature **442,** 766 (2006).

[39] H. Hirata and M. Ono, Resonance frequency estimation of a bridged loop-gap resonator used for magnetic resonance measurements, Rev. Sci. Instrum. **67,** 73 (1996).

[40] S. Petryakov, M. Chzhan, A. Samouilov, G. He, P. Kuppusamy, and J. L. Zweier, A bridged loop-gap S-band surface resonator for topical EPR spectroscopy, J. Magn. Reson. **151,** 124 (2001).

[41] W. Piasecki and W. Froncisz, Field distributions in loop-gap resonators, Meas. Sci. Technol. **4,** 1363 (1993).

[42] See Supplemental Material at http://link.aps.org/supplemental/10.1103/PhysRevApplied.15.034082 for examples of the microwave simulation code.

[43] Q. Zhang and H. Li, MOEA/D: A multiobjective evolutionary algorithm based on decomposition, IEEE Trans. Evolution. Comput. **11,** 712 (2007).

[44] H. Li and Q. Zhang, Multiobjective optimization problems with complicated pareto sets, MOEA/D and NSGA-II, IEEE Trans. Evolution. Comput. **13,** 284 (2009).

[45] G. R. Eaton, S. S. Eaton, D. P. Barr, and R. T. Weber, *Quantitative EPR* (Springer-Verlag, Wien, 2010).

[46] M. Widmann, S.-Y. Lee, T. Rendler, N. T. Son, H. Fedder, S. Paik, L.-P. Yang, N. Zhao, S. Yang, I. Booker, A. Denisenko, M. Jamali, S. A. Momenzadeh, I. Gerhardt, T. Ohshima, A. Gali, E. Janzén, and J. Wrachtrup, Coherent control of single spins in silicon carbide at room temperature, Nat. Mater. **14,** 164 (2015).

[47] S. G. Carter, O. O. Soykal, P. Dev, S. E. Economou, and E. R. Glaser, Spin coherence and echo modulation of the silicon vacancy in $4H-\mathrm{SiC}$ at room temperature, Phys. Rev. B **92,** 161202(R) (2015).

[48] L. Childress, M. V. Gurudev Dutt, J. M. Taylor, A. S. Zibrov, F. Jelezko, J. Wrachtrup, P. R. Hemmer, and M. D. Lukin, Coherent dynamics of coupled electron and nuclear spin qubits in diamond, Science **314,** 281 (2006).

[49] G. de Lange, T. van der Sar, M. Blok, Z.-H. Wang, V. Dobrovitski, and R. Hanson, Controlling the quantum dynamics of a mesoscopic spin bath in diamond, Sci. Rep. **2,** 382 (2012).

[50] T. Gaebel, M. Domhan, I. Popa, C. Wittmann, P. Neumann, F. Jelezko, J. R. Rabeau, N. Stavrias, A. D. Greentree, S. Prawer, J. Meijer, J. Twamley, P. R. Hemmer, and J. Wrachtrup, Room-temperature coherent coupling of single spins in diamond, Nat. Phys. **2,** 408 (2006).

[51] C. S. Shin, D.-K. Qing, Z. Deng, and P. R. Hemmer, Enhancement of electromagnetic fields with subwavelength microwave resonators, Phys. Rev. B **72,** 193102 (2005).

[52] X. Zhang and Z. Liu, Superlenses to overcome the diffraction limit, Nat. Mater. **7,** 435 (2008).

[53] M. A. Al-Joumayly and N. Behdad, Wideband planar microwave lenses using sub-wavelength spatial phase shifters, IEEE Trans. Antennas Propag. **59,** 4542 (2011).

[54] A. Grbic and G. V. Eleftheriades, Subwavelength focusing using a negative-refractive-index transmission line lens, IEEE Antennas Wirel. Propag. Lett. **2,** 186 (2003).

[55] A. Grbic and G. V. Eleftheriades, Overcoming the Diffraction Limit with a Planar Left-Handed Transmission-Line Lens, Phys. Rev. Lett. **92,** 117403 (2004).

[56] P. A. Belov, Y. Hao, and S. Sudhakaran, Subwavelength microwave imaging using an array of parallel conducting wires as a lens, Phys. Rev. B **73,** 033108 (2006).

[57] T. Takakura, M. Pioro-Ladrière, T. Obata, Y.-S. Shin, R. Brunner, K. Yoshida, T. Taniyama, and S. Tarucha, Triple quantum dot device designed for three spin qubits, Appl. Phys. Lett. **97,** 212104 (2010).

[58] J. Yoneda, T. Otsuka, T. Takakura, M. Pioro-Ladrière, R. Brunner, H. Lu, T. Nakajima, T. Obata, A. Noiri, C. J. Palmstrøm, A. C. Gossard, and S. Tarucha, Robust micromagnet design for fast electrical manipulations of single spins in quantum dots, Appl. Phys. Express **8,** 084401 (2015).

[59] C. Geuzaine and J.-F. Remacle, Gmsh: A 3-D finite element mesh generator with built-in pre- and post-processing facilities, Int. J. Numer. Methods Eng. **79,** 1309 (2009).

[60] J. Keranen, J. Pippuri, M. Malinen, J. Ruokolainen, P. Raback, M. Lyly, and K. Tammi, Efficient parallel 3-D computation of electrical machines with elmer, IEEE Trans. Magn. **51,** 1 (2015).

[61] T. B. A. Senior, Impedance boundary conditions for imperfectly conducting surfaces, Appl. Sci. Res., Sect. B **8,** 418 (1960).